Plasma Physics and Controlled Fusion

PAPER • OPEN ACCESS

From minimum-viable-products to full models: a step-wise development of diagnostic forward models in support of design, analysis and modelling on the ST40 tokamak

To cite this article: Marco Sertoli *et al* 2024 *Plasma Phys. Control. Fusion* **66** 095011

OPEN ACCESS
IOP Publishing
Plasma Physics and Controlled Fusion
Plasma Phys. Control. Fusion **66** (2024) 095011 (15pp)
https://doi.org/10.1088/1361-6587/ad668f

From minimum-viable-products to full models: a step-wise development of diagnostic forward models in support of design, analysis and modelling on the ST40 tokamak

Marco Sertoli[1,*], **A Alieva**[1], **P F Buxton**[1], **A Dnestrovskii**[1], **M Gemmell**[1], **H Lowe**[1], **T O'Gorman**[1], **D Osin**[1], **A Sladkomedova**[1], **J Varje**[1], **H V Willett**[1], **J Wood**[1], **Bart A Lomanowski**[2], **E Delabie**[2], **O Marchuk**[3], **E Litherland-Smith**[4], **K Collie**[4], **S Gadgil**[4] **and the Tokamak Energy Team**[5]

[1] Tokamak Energy Ltd, 173 Brook Drive, Milton Park, Oxfordshire OX14 4SD, United Kingdom
[2] Oak Ridge National Laboratory, Oak Ridge, TN 37831, United States of America
[3] Institute of Fusion Energy & Nuclear Waste Management - Plasma Physics Forschungszentrum Jülich, Jülich 52425, Germany
[4] UKAEA, Culham Centre for Fusion Energy, Culham Science Centre, Abingdon, Oxon OX14 3DB, United Kingdom

E-mail: marco.sertoli@tokamakenergy.com

Received 2 April 2024, revised 14 June 2024
Accepted for publication 19 July 2024
Published 2 August 2024

Abstract

Like most magnetic confined fusion experiments, the ST40 tokamak started off with a small subset of diagnostics and gradually increased the diagnostic set to include more complex and comprehensive systems. To make the most of each operational phase, forward models of various diagnostics are used and developed to aid design, provide consistency-checks during commissioning, test analysis methods, and build workflows to constrain high-level parameters to inform interpretation, theory and modelling. For new models and new analysis workflows, minimum-viable-products are released early, and their complexity is increased in a step-wise manner, facilitating the support of all programme phases on multiple parallel applications, while enabling learning opportunities and feedback loops. In this contribution we review the philosophy, scope and architecture of the framework under development. We discuss the details of some forward models, with examples on how they are used to aid diagnostic design, to investigate analysis methodologies through synthetic data, and how they are embedded in

[5] See McNamara *et al* 2023 (https://doi.org/10.1088/1741-4326/acbec) for the Tokamak Energy Team.
[*] Author to whom any correspondence should be addressed.

experimental analysis workflows. We compare previously published experimental results with new, more advanced analysis workflows employing more recent, detailed models and new diagnostic data, providing confirmation of the published material from the 2021–22 experimental campaign.

Keywords: magnetic confined fusion, experimental plasma physics, diagnostics, data analysis, integrated data analysis, forward models, inference

1. Introduction

The characterisation of fusion plasmas requires a comprehensive set of diagnostic systems measuring a wide range of parameters. New experiments typically start off with a small subset of simple diagnostics and gradually increase their measurement capability to include more complex and comprehensive systems. This is sensible given design, procurement, and commissioning of machine and diagnostics is time and resource demanding, and is always a learning process. Additionally, since the different phases of machine commissioning necessitate different levels of measurement coverage, roll-out of diagnostic systems can be planned in phases, with primary systems installed and commissioned early, and the rest rolled out in subsequent waves.

On the ST40 high-field spherical tokamak [1], built and operated by Tokamak Energy Ltd forward models of various diagnostics are being used to support and make the most of each operational phase, aiding diagnostic design, providing consistency-checks during commissioning, testing analysis methods, and building workflows to constrain high-level parameters. Given the wealth of tools previously developed by the fusion community for this purpose (see e.g. [2–17]) it is vital to make the most of this wealth of knowledge, avoid reinventing the wheel, and contribute to these widely used, developed, and maintained projects. This of course applies to those tools that are either open-source or for which collaboration frameworks are already in place, which includes e.g. Open-ADAS [7] for atomic data calculations and spectroscopy, FIDASIM [5, 18] for neutral beams injectors (NBI) and charge exchange recombination spectroscopy (CXRS) modelling [19], CHERAB [4] for H_α camera model [20], ASCOT for the neutral particle analyser (NPA). Everything else that is not accessible must be developed in-house so that the programme can move at pace while new collaboration agreements are being discussed.

The open-source projects listed above will not be discussed in this publication, since they are well known in the community and are used within their well documented capabilities at Tokamak Energy. This contribution will instead concentrate a the in-house developments of a new framework for general purpose diagnostic forward modelling called *Indica*. We will give an overview of the general architecture of the project (section 2) and share examples of the diagnostic forward models, discussing how they are used to aid diagnostic design and test analysis methodologies using synthetic data (section 3). We show how they have been applied to analyse ST40 experimental data, comparing previously published results with results of new, upgraded analysis workflows applied to the same dataset, as well as applying old workflows to recent experiments where an upgraded set of diagnostics was available (section 4). An outlook and plans for the future are given in section 5.

2. Overview of the framework

Indica is a general purpose framework for diagnostic forward modelling and integrated diagnostic analysis workflows [21]. It is currently written 100% in Python, and has an open source *GPL3.0* license to embed collaborative development at its core and leave the door open for expressions of interest from the community as a whole, both from public or private actors. The package is still under development, and is due to be released soon and can be found at https://github.com/indica-mcf/Indica. All the results and graphs in this publication have been produced using the code from its *main* branch.

Within *Indica*, forward models are developed giving special attention to readability, simplicity, and modularity, key to a cyclic, agile development process. Minimum-viable-product (MVP) models are released early and tested on synthetic data and live analysis workflows. If the boundary conditions for the model application are well defined, their inclusion in analysis and modelling chains can provide valuable information to streamline decision-making, facilitating multiple parallel applications, learning opportunities and feedback loops. Successive releases can then expand the boundary conditions, provide a benchmark for previous versions, informing among other things what approximations can be retained and what complexity is necessary for an accurate (enough) characterisation of the measurements.

2.1. Diagnostic models

A diagnostic object is built based on its measurement principles, e.g. Thomson scattering, passive or active spectroscopy, soft x-ray (SXR) cameras, etc and is instantiated setting the attributes defined by the experimental setup. A *Geometry* object takes care of interpolating and integrating quantities along lines-of-sight (LOS) or at the measurement locations, and interfaces with an *Equilibrium* object to perform conversions between Cartesian and flux space.

Each model is equipped with additional methods to compute quantities relevant for the characterisation of the diagnostics measurements and the output of its call is the expected measured quantities. This is organised in the same format as data read from the experimental database to ease the

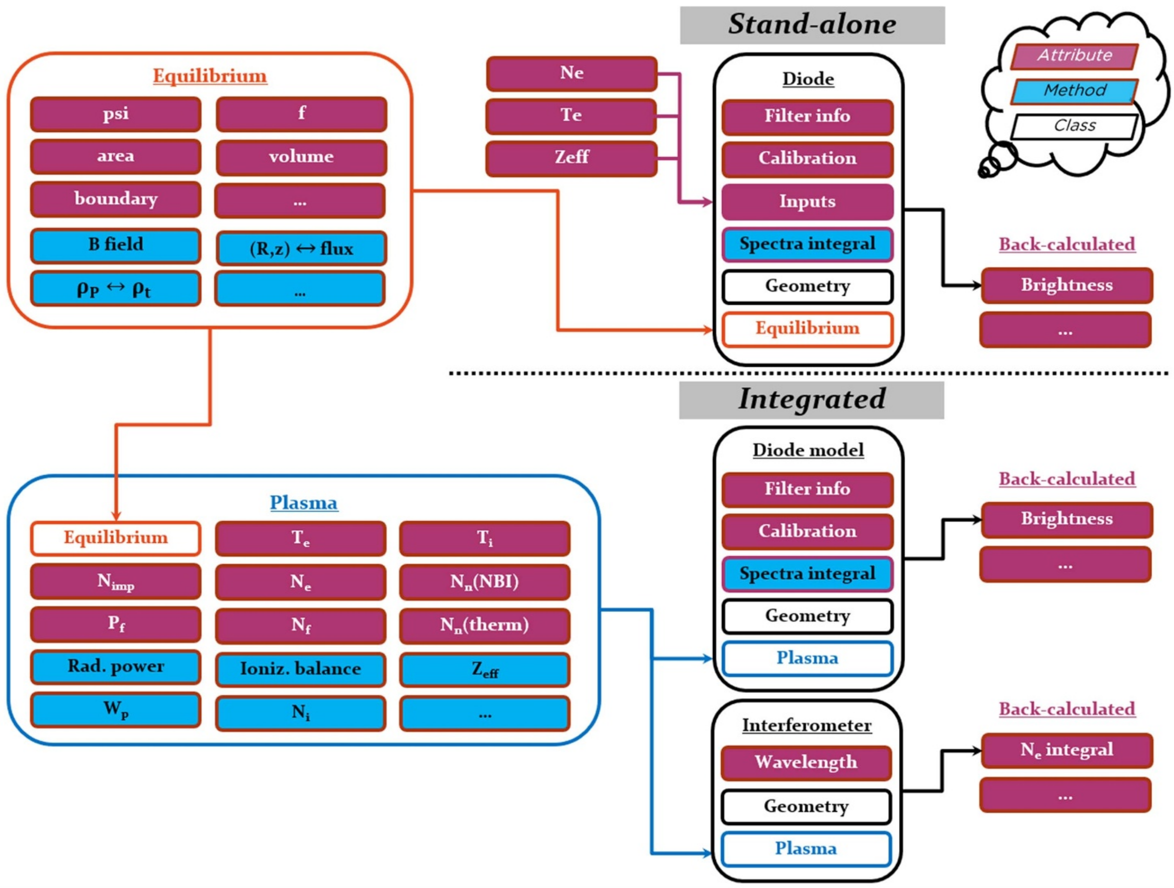

Figure 1. Workflows to run diagnostic forward models stand-alone (top) or integrated using a common plasma model (bottom).

comparison, plotting and inclusion in optimisation workflows, reducing additional coding to the minimum. Where preexisting diagnostic models from other projects are used, their output is reorganised in the same format so they can be used in exactly the same manner.

As an example, a simple diode equipped with an interference filter aimed at measuring Bremsstrahlung radiation in the visible range will, in its simplest form, be defined by the details of the filter's central wavelength, width, and shape. The arguments of its call will be the electron density, temperature and effective charge profiles, and its output the expected measured Bremsstrahlung brightness (following equation (2) from [22]). Additional methods include the capability to integrate the spectra of a grating spectrometer convoluting it with the diode filter function, providing a straightforward way to compare different diagnostics.

2.2. Workflows

Models can be used stand-alone or in an integrated manner (figure 1). When used on their own, the inputs are designed to be at the lowest possible/reasonable level to retain a physical meaning while avoiding unnecessary extra calculations. When run in an integrated manner all the quantities necessary to run the objects are delivered through a common *Plasma* object. Independent quantities (e.g. electron density and temperature, impurity density, toroidal rotation, etc) can be set by the user, while derived quantities (e.g. mean charge, main ion density, etc) are read-only *Python properties* which are self-consistently calculated and cached whenever the independent variables change. In the spirit of modularity and readability, general physics equations are collected in separate files so to be available for multiple independent applications.

Using this basic information, any sort of optimisation workflow can be constructed. These include adapting coverage and number of channels in the design phase of a single diagnostic to optimise for a specific output, developing inference procedures of plasma profiles (radiation or kinetic), cross-correlating different diagnostics measuring the same quantity, and many more. Some examples of the available models and applications are explained in the next section.

3. Diagnostic design and analysis methodologies

3.1. Total radiated power

As first example, a tangential bolometer array viewing the *xy*-plane on the midplane is modelled to assess its potential, sensitivity and capabilities. The analysis is performed on a purely synthetic dataset (referred to as *phantom* from now on): the ST40 equilibrium with $R_{mag} \sim 0.5\,\mathrm{m}$ and $a \sim 0.3\,\mathrm{m}$, plasma electron temperature profiles with $T_e(0) = 3\,\mathrm{keV}$

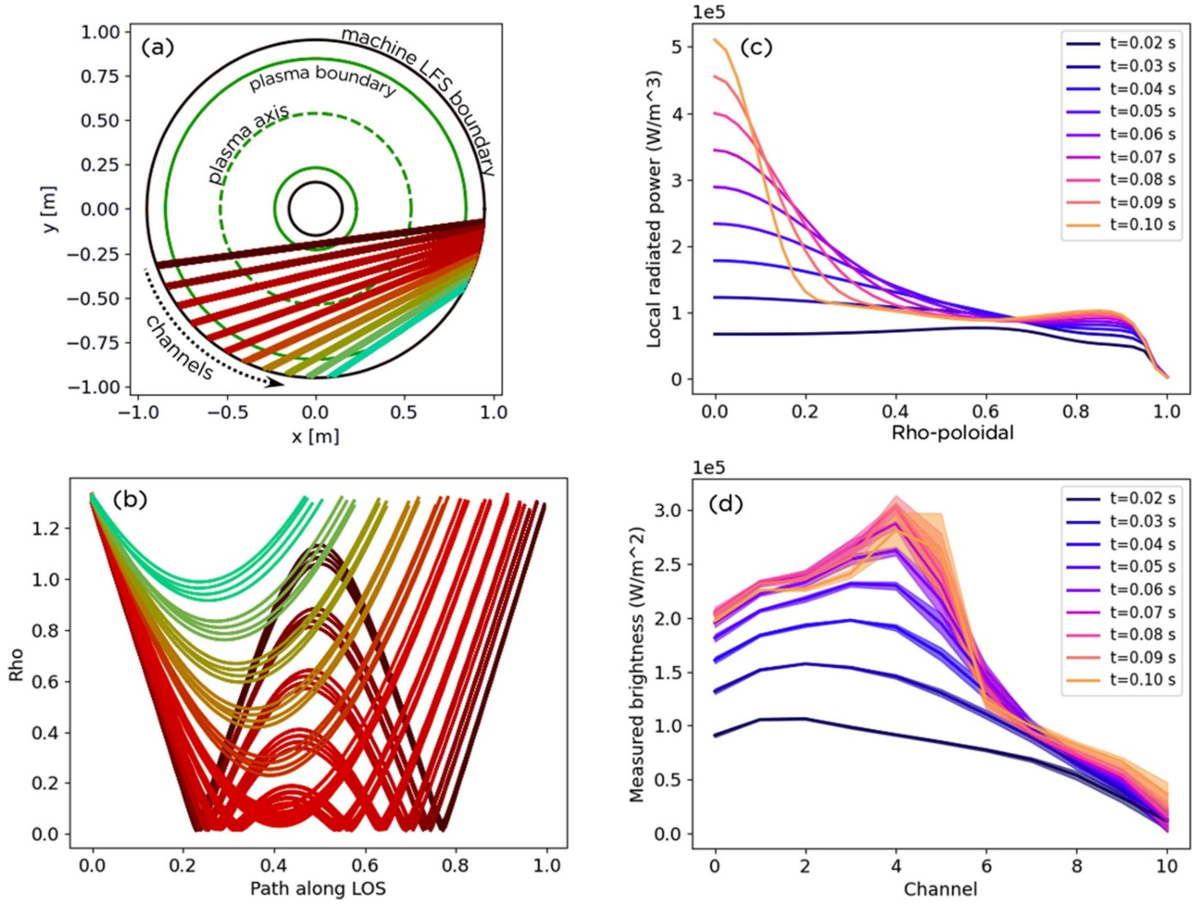

Figure 2. Bolometer diagnostic model: (a) viewing geometry projection on the *xy*-plane and (b) LOS path across the plasma vs. normalised poloidal flux (different LOS have different colours, different lines of the same colour represent beamlets of the same LOS); (c) phantom local total radiated power, (d) resulting measured brightness (same colour code as in (c). Shaded bands in d represent upper and lower bounds measured by the different beamlets, the thick continuous line is the average value.)

(see figure 5(a), electron density with $N_e(0) = 5 \times 10^{19}\,\mathrm{m}^{-3}$, background carbon concentration of 2% similar to what is observed on other C-wall spherical tokamaks [23, 24] and reasonable argon concentrations of 0.1%. An argon impurity accumulation event is then simulated increasing its density peaking in time. The total radiated power is calculated using atomic data from Open-ADAS [7], computing the ion fractional abundance using ionisation, recombination and charge-exchange rates, and including line and recombination radiation to compute the cooling factors. The resulting increase in the local radiated power profile is shown in figure 2(c), plotted vs. the normalised poloidal flux coordinate rho-poloidal $\rho_{pol} = \sqrt{(\psi - \psi_a)/(\psi_s - \psi_a)}$, where ψ is the poloidal flux and the indices s and a refer to the separatrix and magnetic axis respectively.

The viewing geometry is chosen to cover the whole plasma from the low-field-side (LFS) to the high-field-side (HFS) boundary with a total of 11 channels (figure 2(a)). Finite line-of-sight (LOS) width effects are modelled using a set of beamlets, i.e. independent infinitely small LOS distributed uniformly in Cartesian space within pre-defined viewing cones. Various possible geometries can be implemented to simulate visible spectroscopy, pinhole cameras, NBI, etc. As an example, the LOS in figure 2(b) have been modelled using 16 beamlets and a cylindrical spot size of 3 cm diameter. The path along the flux surfaces of the various beamlets, where different beamlets of the same LOS are shown as different lines of the same colour (LOS have the same colour coding as in figure 2(a). Using one beamlet will revert to a standard pencil-like, infinitely small line-of-sight approximation.

The resulting back-calculated brightness is shown in figure 2(d) (same colour coding as figure 2(c). The shaded area shows the variability of the LOS-integral for the different beamlets, while the continuous line is the average over all beamlets. As expected, LOS-width effects matter most for regions of the plasma where the gradients are large in comparison to the LOS width for those channels viewing these regions tangentially, in this case the most centrally and edge LOS. This can be particularly important on ST40 given the small plasma size, the extreme gradients and the short pulse lengths.

For diagnostic design applications, the model can be extended to include calibration constants and conversion factors to compute the expected raw signal (e.g. in *volts* or *Amperes* or *counts*), providing valuable information to inform design (e.g. the expected signal-to-noise ratio). If the main interest is instead to test analysis techniques, the output of the model can

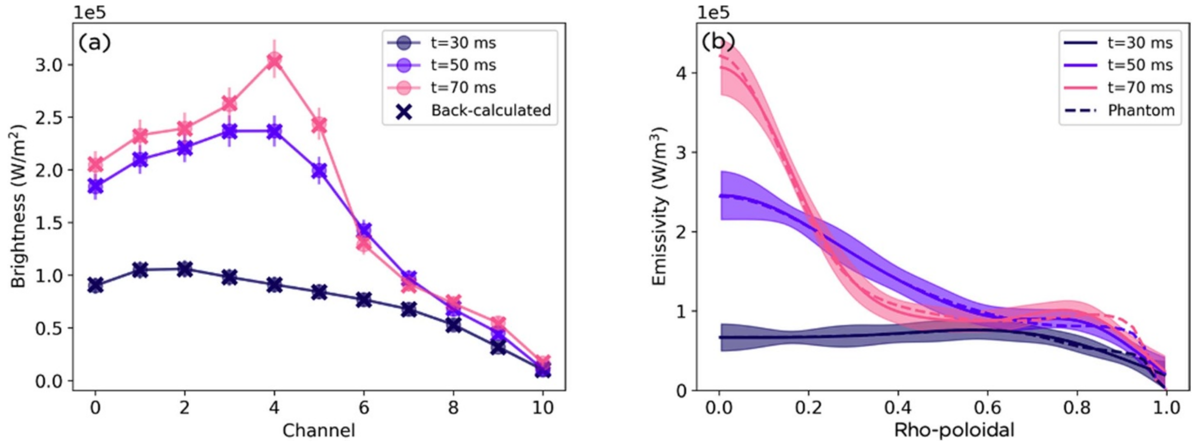

Figure 3. Inversion of bolometer brightness from figure 2: (a) comparison of the phantom brightness (circles) and back-calculated values (crosses), (b) comparison of the phantom (dashed lines) and the inverted local emissivity (continuous lines and shaded error band). Refer to figure 2(a) to relate channel # to LOS geometry.

be fed into independent methods/packages to test how well the back-calculated values match the ground truth of the quantity being measured.

Figure 3 shows the application of a 1D tomography code [25] to compute the total radiated power from the LOS-integrals of the phantom bolometer diagnostic from figure 2. The inversion routine works extremely well in recovering the phantom profiles (dashed lines in figure 3(b) for a wide range of peaking of the local emissivity profiles, which is reflected in the good match between the back-calculated LOS-integrals and the phantom bolometer data (figure 3(a), crosses and circles respectively). If these tests are performed during the diagnostic's design phase, they can substantiate (or not) the design parameters and inform modification of the LOS geometry or number of channels required to reconstruct the expected radiation profiles. If the system is already installed, this phantom analysis provides important information on the boundary conditions for the validity of use of the chosen inversion technique or optimisation parameters used, for which alternative solutions can be sought.

In the case of strongly rotating plasmas where the radiation can be in-out asymmetric due to centrifugal effects [26], a 1D inversion assuming poloidal symmetry on a flux surface is not suitable, nor are 2D tomographic methodologies if only a tangential camera as is available, as in the example geometry used for the bolometer diagnostic (figure 2). For this application, model-driven inference techniques similar to those developed in [27, 28] can be used instead, with the 2D local emissivity map on the (R,z) plane reconstructed optimising the profile shapes of a symmetric emissivity and an asymmetry parameter (see equation (1) in [27]). An example of this is shown in figure 4, using again the same plasma parameters as in figure 2, but adding toroidal rotation to generate the poloidal asymmetry following Wesson's formula [26]. The inference procedure, while extremely simple in its functional form, is extremely successful in recovering the phantom 2D emissivity, as is clear when comparing the 2D maps (figures 4(c) and (d) and the midplane cut at $z=0$ (figure 4(b)). If up-down asymmetries can be neglected, such an analysis methodology can provide a reliable way of inferring poloidally asymmetric radiation profiles without tomography-capable diagnostics that typically require a very large number of cameras and lines-of-sights viewing from different angles.

A word of caution is necessary at this stage, as it must be clarified that the number of LOS, the SNR achieved by the system, the precision of the equilibrium reconstruction will all play a major role in the quality of these analyses. The impact of these uncertainties are not investigated in this paper, but should be included in in-depth phantom analysis on any system, existing or future.

3.2. Passive spectroscopy

Another diagnostic and model widely used in the community is that of the x-ray crystal spectrometer (XRCS) measuring the He-like argon spectral lines at ~ 0.4 nm (see e.g. [29–33]). This diagnostic has been extensively developed and applied on many fusion devices, and can provide information on both electron and ion temperatures, argon concentration and neutral densities. If set up with spatially resolved capabilities [30], these quantities can also be locally resolved using inversion or inference methodologies. Figure 5 shows an example of the output of the model using the geometry in figure 2(a), as well as the same argon accumulation scenario and local plasma parameters for the bolometer example.

While this set-up is desirable, on ST40 the XRCS is equipped with a single radial-midplane LOS. The diagnostic and model was nonetheless extensively used to constrain the temperature profiles during the 2021–22 ST40 experimental campaign when no profile capable diagnostics were available. Back then, the model itself was in its infancy, with only with information on the emissivity characteristics of the He-like resonance line w [7]. As will be clear in the next sections, despite these limitations, including the model in optimisation workflows to constrain the electron and ion temperatures using moment analysis techniques (see equation (8) of [31]) was highly successful.

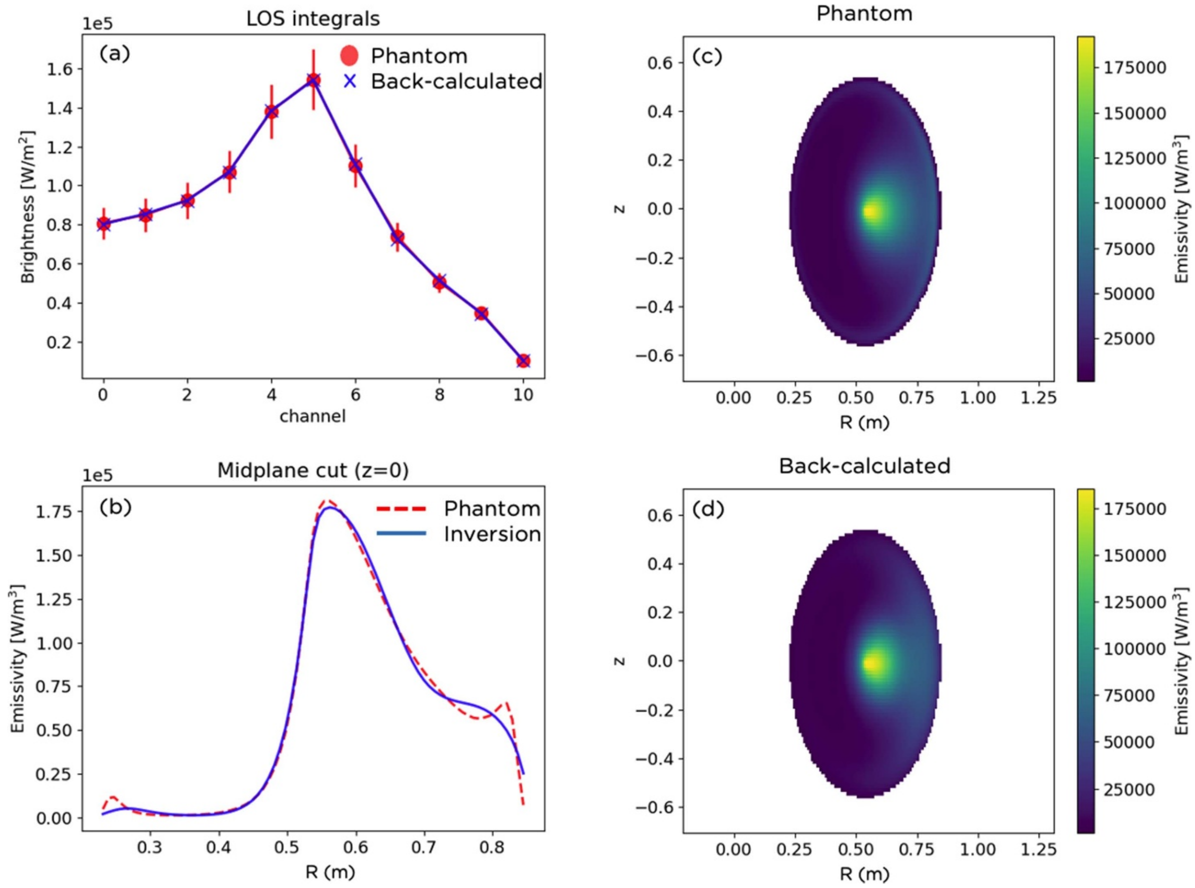

Figure 4. Inference of the 2D poloidal map of the total radiation using the same phantom plasma data and bolometer model from figure 2. (a) Phantom brightness vs back-calculated values (circles and crosses), (b) midplane cut at $z = 0$ of the phantom and inferred radiation distribution (dashed and continuous lines), phantom (c) and back-calculated (d) 2D poloidal map of the radiation.

3.3. Active spectroscopy

Another standard diagnostic present on most tokamaks that are equipped with neutral beam injection (NBI) systems, is the charge exchange recombination spectroscopy (CXRS) (see e.g. [34] and references therein). The model for this diagnostic has been implemented employing FIDASIM for the NBI modelling and computing the expected active spectra including both Doppler widths and shifts.

On ST40 this model has not yet been directly used in optimisation workflows, but to investigate the limitations of the diagnostic geometrical set-up. Due to space constraints, it was not installed in an optimal viewing geometry for full profile coverage, with all the LOS tangential to the flux surfaces at the intersection with the neutral beam. It was instead optimised for a view of the plasma centre at $R \sim 0.4 - 0.6\,\mathrm{m}$ (figure 6(a)) so could be subject to temperature smearing and rotation shearing further away from these radii which could lead to an overestimation of the local values.

Detailed sensitivity studies have been undertaken to assess the level of this non-localisation of the two systems currently installed [19, 35] which will be referred to as TWS and PI as labelled in figure 6(a). Using phantom plasma parameters to quantitatively investigate the systems' limitations, the back-calculated active spectra was fitted with the same routine used on the experimental data. To be more complete, phantom passive lines were included in the model as well, also scanning the active/passive ratio for completeness. The results are shown in figures 6(c) and (d), the dashed line representing the local values of temperature and rotation, while the symbols show the expected measurement from fit of the spectra, with x-axis position representing the intersection point between the LOS and the centre of the NBI. The pink squares and blue circles show the two systems as installed during the latest 2023 campaign.

It can be clearly seen how the local ion temperature and toroidal rotation are overestimated for $R > 0.6\,\mathrm{m}$, with the outermost radial point from PI overshooting by $\sim 1\,\mathrm{keV}$. The forward model has been further applied to H-mode-like profiles with ion temperature pedestal to investigate whether inference procedures could help recover the local values, but only negligible changes in the measured ion temperature would be observed, thus not justifying the effort in pursuing this analysis further. While alternative viewing geometries are being explored and modelled, the TWS geometry for the 2024 campaign has been upgraded to provide one more radial point as far to the LFS as possible (yellow crosses in figures 6(c) and (d)) to support the next phase of operation and expand the analysis workflows for the inference of ion temperature profiles.

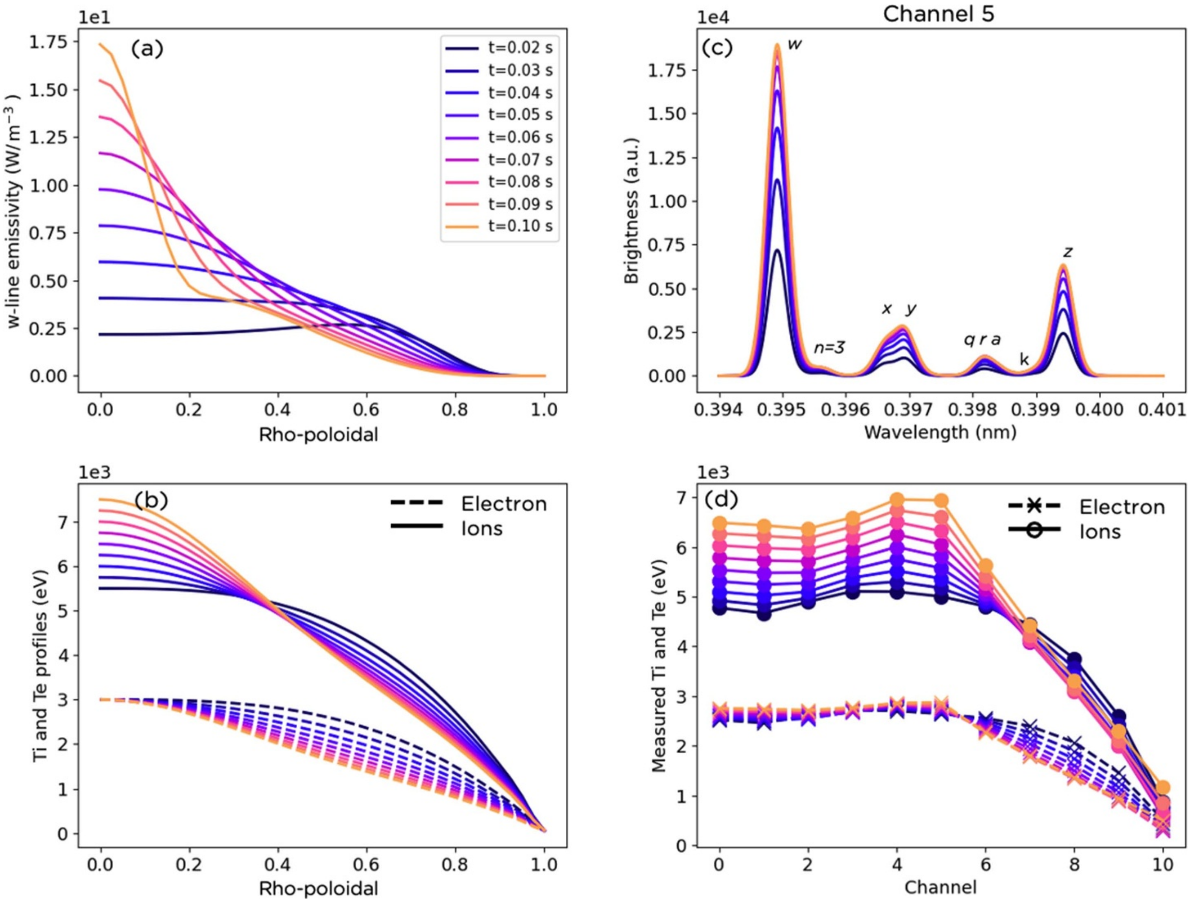

Figure 5. XRCS forward model results using the same phantom plasma data and LOS geometry from figure 2: (a) local emissivity of the He-like Ar resonance line *w*; (b) phantom ion and electron temperatures; (c) back-calculated He-like Ar spectra (main resonances and satellites labelled); (d) back-calculated ion and electron temperatures along the different LOSs using the moment analysis technique.

3.4. Visible Bremsstrahlung

If absolutely calibrated, the CXRS system can also provide information on the plasma composition. The active intensity of the active component of the spectra can be related to the concentration of the measured impurity ion and the plasma effective charge (Zeff) can be computed from spectral regions free from line emission employing the same equation used for the Bremsstrahlung diode discussed previously. If this measurement is performed along several lines of sight, a Zeff profile can be computed using inversion or inference algorithms [36, 37]. Both inference and inversion methods have been implemented and tested using phantoms to investigate the sensitivity of the results to the diagnostic geometry [38]. Using the same LOS geometry and plasma parameters as for the other models in this section (figure 2) the Zeff profile (figure 7(b)) has been computed inverting the LOS-integrals of the Bremsstrahlung emission (figure 7(a)) using the same inversion routine applied to the bolometer (figure 3). The methodology recovers well the shape of the phantom Zeff profiles (dashed lines) even for the extreme peaking ($t = 70$ ms), but the uncertainty from the inversion propagated to the effective charge calculation leads to a relatively wide Zeff confidence band. Moreover, this is a lower bound of uncertainty since errors on the electron temperature and density have not propagated. More work has been done on this in [38] and will be published in a separate paper.

4. Experimental results and analysis workflows

In this section, we look at the analysis workflows developed in 2021–22 for the scope of constraining the central hydrogenic ion temperature which was a 2022 business milestone. We compare the published results [1] with the results from newer models and upgraded analysis workflows, and test the output of old workflows against new experimental data from 2023. Before diving into the comparison, it is worth giving an overview of the experimental results and outline the measurement availability of the ST40 tokamak during that campaign.

The diagnostic set available during the 2021–22 campaigns did not include any profile-capable diagnostics. Most of the measurements were performed on single lines of sight viewing from the LFS midplane with the exception of a tangential SXR camera viewing vertically across the plasma from the LFS midplane and a few lines of sight of CXRS spectrometers centred around the plasma axis. The electron density was measured using a sub-millimetre (SMM) interferometer, the electron temperature using the XRCS He-like passive spectra

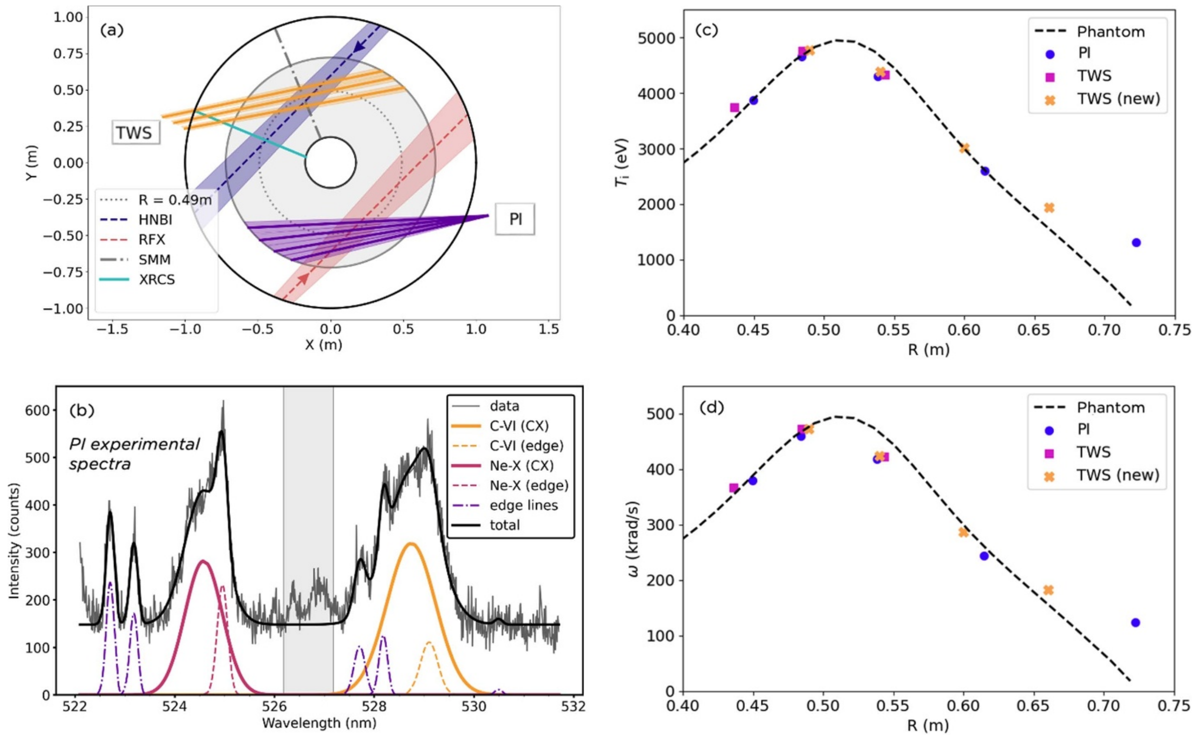

Figure 6. (a) viewing geometry of the CXRS systems (PI and TWS), XRCS spectrometer, SMM interferometer, NBI injectors (RFX and HNBI) during the 2021–22 experimental campaign; (b) experimental CXRS spectra from the centrally-viewing LOS for pulse 10 009 at 60 ms, active (CX) and passive (edge) components labelled. CXRS forward model results (symbols) compared to the phantom profiles (dashed lines) of ion temperature (c) and toroidal rotation (d).

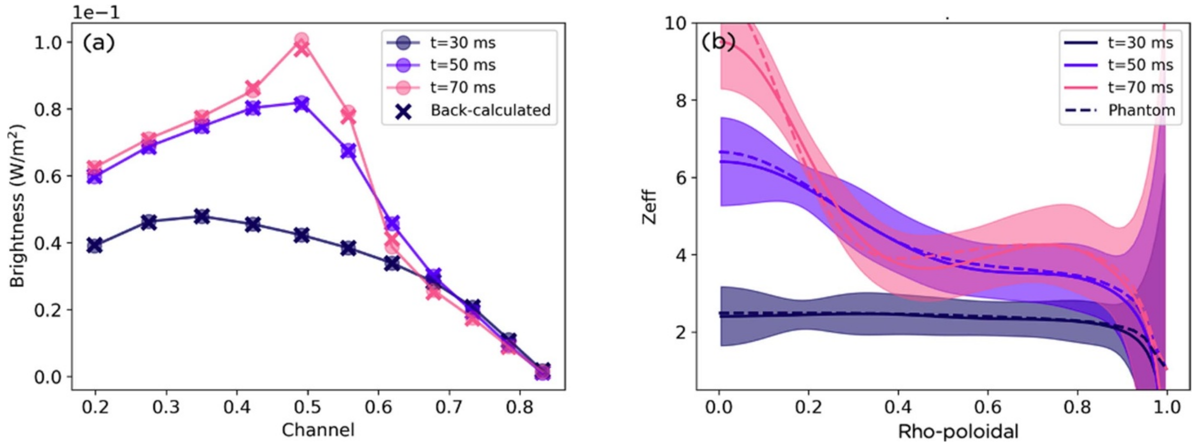

Figure 7. Phantom analysis of Zeff profile calculation inverting the Bremsstrahlung signal measured by passive visible spectroscopy at $\sim$530 nm using the same phantom plasma data and LOS geometry of the bolometer model from figure 2. (a) comparison between phantom brightness and back-calculated values from the inversion (circles and crosses), (b) comparison between phantom Zeff profile and the profile calculated from the inverted Bremsstrahlung emissivity (dashed lines and continuous lines with shaded error band).

line ratios, the ion temperature from the XRCS spectra and from the active CVI spectra of the PI CXRS spectrometer (see figure 6(a) for LOS geometry). Radiation diagnostics included a single soft x-ray diode detector and a H/Dα filtered diode measuring along single radial LOS at $z = 0$, and a vertical/tangential SXR camera. The time evolution of experimental measurements for a set of pulses from the 2021–22 campaign are shown in figure 8. Clearly observable are sawtooth crashes in the SMM, SXR and Hα filter time traces for pulse 9520; ELM signatures in the Hα for 9783 with a concurrent increase of the line-averaged electron density and radiated power. Pulses 9783 and 10 009 show some of the highest ion temperatures achieved on ST40, with the XRCS spectrometer measuring 8 keV, and the CXRS diagnostic measuring above 9 keV. Key to these high ion temperatures was the switch from hydrogen to deuterium of both gas puff and NBI gases which resulted in higher input heating power, and the step in toroidal field from 1.7 to 2 T (at $R = 0.45$ m).

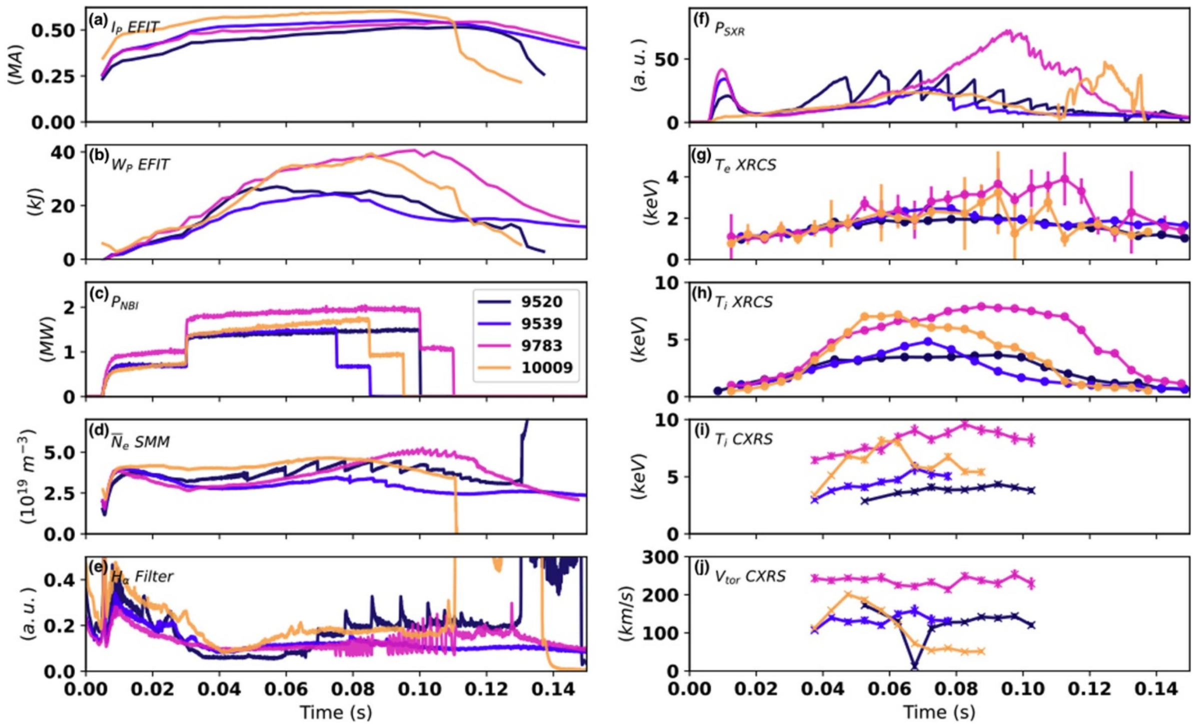

Figure 8. Experimental time traces for a set of 4 representative pulses of the 2021–22 campaign: (a) plasma current, (b) EFIT stored energy, (c) total NBI injected power, (d) SMM LOS-averaged electron density, (e) Hα and (f) SXR brightness, (g) XRCS electron and (h) ion temperature, (i) CXRS ion temperature and (j) toroidal rotation. Pulses 9520 and 9539 were run in full hydrogen (puff and NBI), 9783 with deuterium gas and hydrogen NBI, 10 009 in full deuterium (puff and NBI).

4.1. Constraining the profile shapes

Given the need to validate the central hydrogenic ion temperature (business milestone) with a very limited set of measurements, the choice was taken to perform an integrated analysis of all the available (validated) measurements, and use TRANSP [39] to estimate the central hydrogenic temperatures. With support from modelling to substantiate the underlying assumptions, standard backward diagnostic analyses and inference procedures employing forward models were combined in a step-wise, cyclic optimisation workflow. This was dubbed *hierarchical diagnostic analysis* (HDA), as the most independent measurements are analysed first, progressing then with the more complex quantities dependent on the parameters inferred in the previous steps. The workflow steps have already been discussed in-depth in section 4 of [1] and for the purpose of this publication it is not worth re-explaining them, but a visual representation is shown in figure 9 for completeness. It is instead worth providing some detail on the reasoning that led to the choice of bounds of the profile shapes that were then used in [1, 19, 35, 40–42] which has not been discussed in previous publications.

Peaked density profiles are expected in NBI heated L-modes on ST40 due to the strong core fuelling from the RFX beam. This is confirmed by the sawtooth crashes observed in the SMM interferometer LOS-integrated measurement, in the SXR radiation and the XRCS line intensity, which all indicate peaked electron and impurity density profiles. The tangential SXR camera, despite its poor resolution, also confirms this and provides a rough localisation of the sawtooth inversion radius. Given this information, using a sawtooth crash model which assumes a complete profile flattening inside the inversion radius and particle redistribution over the outer flux surfaces to account for particle conservation, the electron density profile peaking was optimised using the interferometer model attempting to match the observed crash in the measured SMM values. An example of this is shown in figure 10 for the sawtooth crash at $\sim$0.06 s of pulse 9520 (see figure 8), using and inversion radius $\rho_{pol} \sim 0.45$ (corresponding to $r/a \sim 0.4$) estimated from the tangential SXR camera. The broad electron density profile (figure 10(a)) is clearly not peaked enough to explain the experimental drop in interferometer measurement (figure 10(c)), which can be instead be matched using a more peaked electron density profile shape (figures 10(b) and (d)). No constraints are available for the separatrix values, which was set to $0.5 \times 10^{19}\,\mathrm{m}^{-3}$.

Expanding the sawtooth model to include also the argon density, electron and ion temperature profiles, one can also infer the expected XRCS line intensities and the XRCS measured electron and ion temperatures, which can then be compared with experiment. The time evolution of the SXR emission is typically extremely well correlated with that of the XRCS line intensities, also for sawtooth crashes, suggesting the SXR emission is dominated by Ar when this is injected in the plasma. The electron temperature measured by the XRCS is instead approximately constant in time, even during sawtooth crashes, suggesting the electron temperature gradient is relatively shallow inside/close to the sawtooth inversion radius

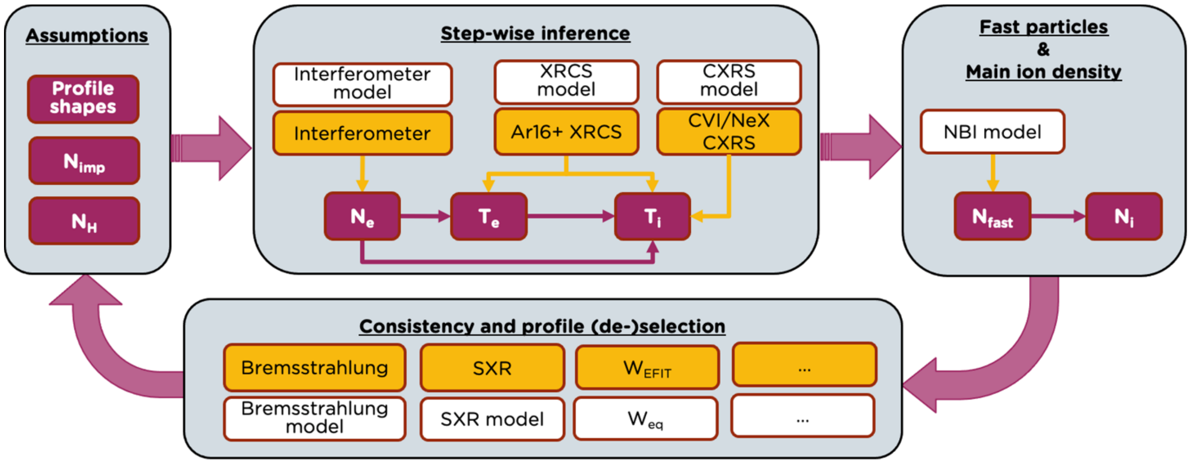

Figure 9. Visual representation of the hierarchical diagnostic analysis (*HDA*) workflow. Refer to section 4 of [1] for an in-depth explanation of the separate steps.

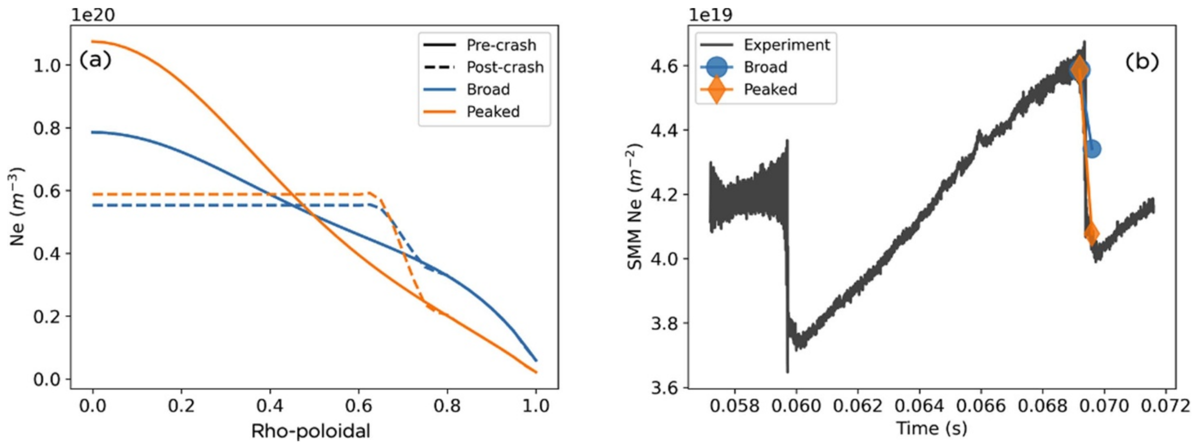

Figure 10. Modelling of a sawtooth crash for pulse 9520 as detected by the SMM interferometer: (a) broad and peaked pre- and post-crash density profiles, (b) response of the SMM interferometer (same colour coding as in (a), experimental data shown in black.

so that the (small) electron temperature crash combined with the change in XRCS measurement position due to the modification of the electron density and argon density profiles has only a minor effect on the line ratios. Broad electron temperature profiles are also suggested by ASTRA [43] and TRANSP [39] modelling attempting to match the measured loop voltage using varying effective charge assumptions. For the ion temperature, the strong crashes observed in the XRCS Ti measurement and the relation between this measurement and the few central CXRS measurements all suggest that the ion temperature profiles are strongly peaked in the inner half of the plasma.

With the reasoning above, peaked electron and impurity density profiles, peaked ion temperature, broad electron temperature profiles have been identified as the most probable kinetic profile shapes for the hot-ion mode scenarios performed during the 2021–22 campaign on ST40. But since the profile shape could not be determined a-priori due to the absence detailed measurements, the final profile sets used in the HDA optimisation workflow included upper and lower bounds of the peaking factors that could then be excluded by the optimisation procedure (figure 11). An additional constraint for the ion temperature profile (figure 11(b)) is the assumption the ion/electron temperature ratio approaches unity at the edge due to higher ion-electron coupling at higher collisionility. For the argon density, the broad argon profile corresponds to a flat concentration (dependent on the electron density assumption), while the profile peaking is higher than that of the electron density, taking into account the conclusions from the sawtooth crash modelling and providing a conservative estimate of the ion and electron temperature measurements by weighing the measurement further in the centre. Additionally, the argon density decay at the edge is imposed to be slower than that of the electrons, accounting for the typically increasing edge effective charge measured on other tokamaks.

All the publications on data from the 2021–22 ST40 experimental campaign [1, 19, 35, 40–42] have used these base profiles and the HDA optimisation workflow using the basic XRCS model ($w - line$ intensity, moment analysis for electron and ion temperatures) and SMM interferometer model

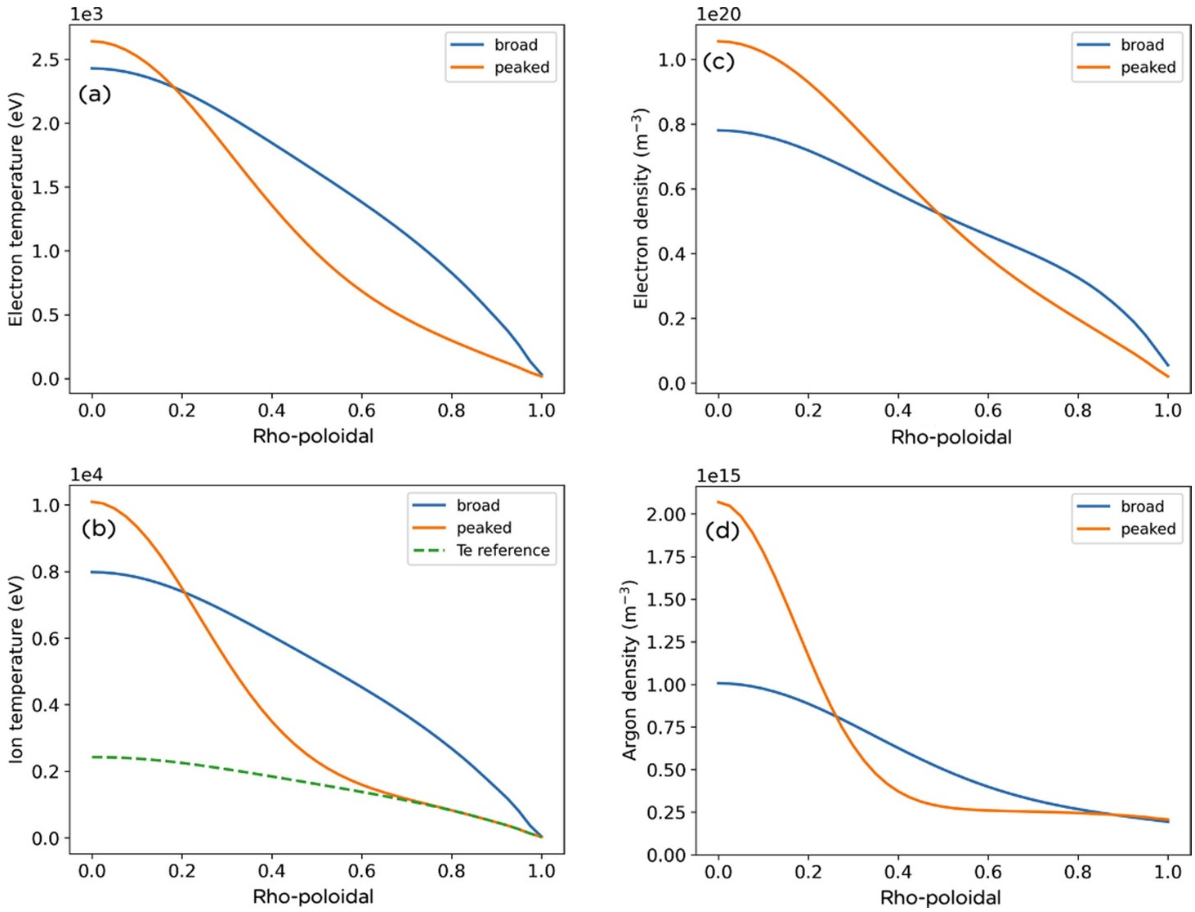

Figure 11. Profile shapes used in the HDA analysis workflow (figure 9): (a) electron temperature, (b) ion temperature, (c) electron density, (d) argon total impurity density.

(no ray-tracing) to constrain the kinetic profiles. The optimisation results for pulse 10 009 at 68 ms as published in [1] are reproduced in figures 12(a) and(b). While the physics assumptions are sound, the experimental observations coherent, and the match with the (limited) experimental data good, even including the (limited) additional information from a few central CXRS measurements and the constraining the total total stored energy vs EFIT using ASTRA/TRANSP to calculate the fast particle contribution, it is clear that this set of profiles can only be used to roughly *constrain* the profile shapes and that more is needed to confirm or refute this early work, both by refining the analysis to be statistically more rigorous, and by testing the results vs profile diagnostics once they would become available.

4.2. Bayesian inference

The analysis workflows have been upgraded in 2023 to enable Bayesian inference of the profile parametrisation (dubbed BDA). Details of the framework will be given in a separate publication, but in this contribution the methodologies have been applied to a set of old discharges to test the the HDA workflow, using broad, flat priors for the profile shape optimisation and the same input experimental data used in the HDA runs. The example given here is a re-analysis of the record hot-ion scenario whose results were published in [1]. In order to be sure to make a sensible comparison, the same experimental data and underlying assumptions have been used, but the latest version of the XRCS model capable of reconstructing the full spectra has been substituted to the basic version used in HDA as described in the previous section. The profiles inferred using BDA are shown in figures 12(c) and (d), and compared to the previous results shown in plots a and b, which come directly from [1]. A total of 15 profile shape parameters have been optimised, enabling the scan over a broad range of profile shapes (light-grey shaded areas). The one sigma (68% confidence) profile shapes inferred using Bayesian inference are consistent with the previous results across all channels, although a slightly higher electron density peaking can be observed, and slightly broader ion temperature profiles. The comparison of the experimental data and the back calculated values for the parameters to be optimised is shown in figure 13. The XRCS spectra has been optimised only in the wavelength range of the resonance line w and the $n3$ satellite. As in the original analysis workflow, a conservative 20% uncertainty has been assumed on all measured quantities.

More could be said and discussed on this comparison if new profile data still was not available. But since new

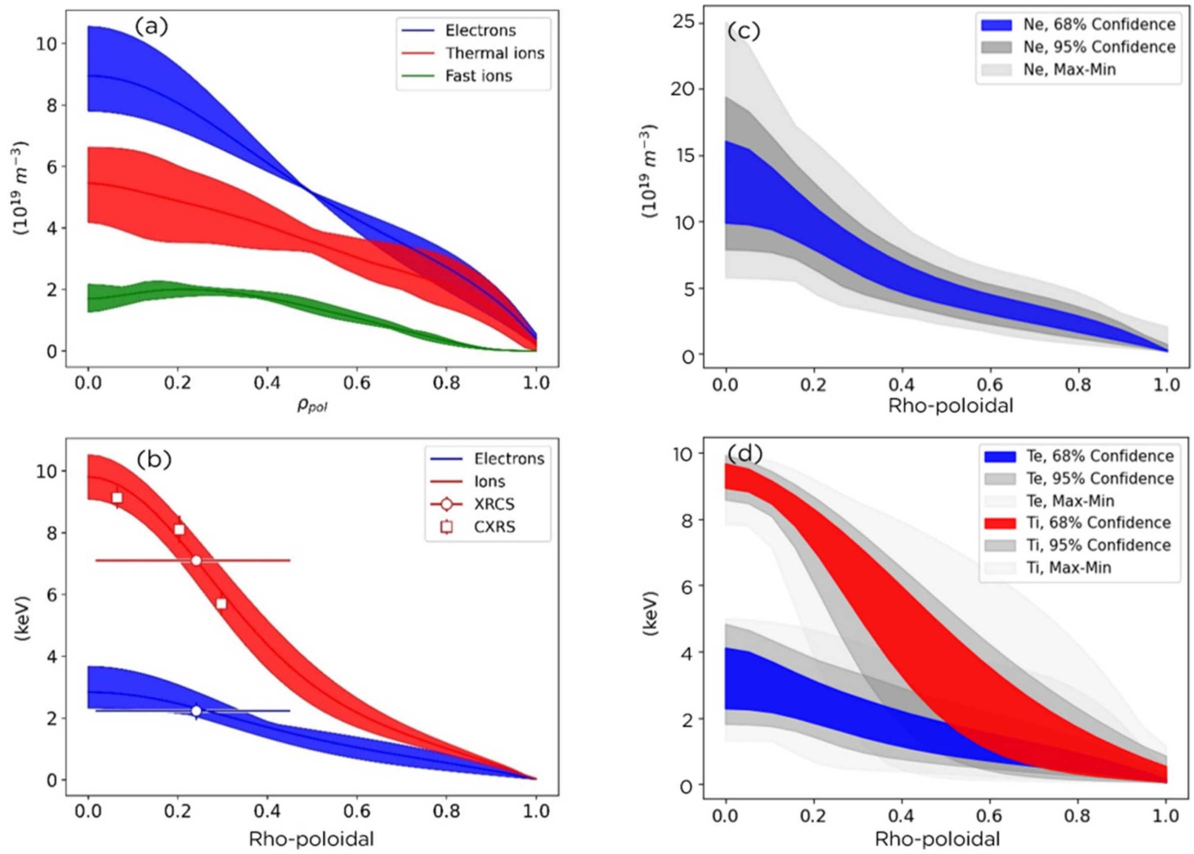

Figure 12. Kinetic profiles for pulse 10 009 at 68 ms computed using (a), (b) the HDA optimisation workflow and (c), (d) the Bayesian inference algorithms, with both analyses methods performed using exactly the same experimental information: EFIT equilibrium reconstruction, XRCS He-like Ar spectra (circles in (b), CXRS CVI 529 nm ion temperature (squares in (b) and SMM interferometer. Comparison of experimental data and BDA back-calculated distributions shown in figure 13. (a, b) Reproduced from [1].

Thomson scattering data has been commissioned during 2023 experimental campaign, it is worth diving straight into the comparison of the HDA results vs TS experimental data.

4.3. Comparison of the HDA results vs Thomson scattering

The ST40 Thomson scattering diagnostic was commissioned in 2023, the details of the system and preliminary results shown in [44–49]. Since the HDA profile shapes had been optimised for limited, hot-ion mode scenarios, a comparison with TS data must be performed on similar scenarios. Three pulses have been chosen for this purpose (11 224, 11 226 and 11 227) as they have very similar geometry to the record hot-ion discharge 10 009 shown in figure 14(d), similar electron density and similarly good XRCS signal-to-noise ratio. Differences include lower plasma current $I_p \sim 0.5\,\mathrm{MA}$ and magnetic field $B_t(R_{geo}) \sim 1.35\,T$, as well as delayed NBI timing (RFX starting at 0.01 s).

The exact same HDA analysis code and assumptions used for 10 009 and described in the previous sections has been run for these discharges. Since the scope of this exercise is to benchmark the optimised profile shapes retained in the analysis of pulses from the previous campaign, the same profile sets as for the 2021–22 hot-ion modes have been retained, without performing any filtering on the plasma stored energy or on the measured CXRS measured central ion temperature. The results are shown in figure 14, mapped to the midplane R so to compare directly vs the measured TS and CXRS values. A 20 ms time window of stable plasma has been chosen to have at least two time-points from both TS and CXRS, both acquiring at 10 ms but at slightly different times (CXRS at 57 and 67 ms, TS at 62 and 72 ms). For all three pulses, the TS electron density data is sitting almost exactly in the middle of the peaked and broad HDA profile bounds. The TS electron temperature is very similar to the broad HDA profile shape, sometimes dipping below this bound, but never reaching the lower HDA bound and confirming the previous conclusion that electron temperature profiles are relatively broad. The CXRS data also corroborates the ion temperature profile shape and central values computed using the HDA analysis. The two TS radial points measuring a dip in electron temperature close to the plasma centre $R \sim 0.55\,\mathrm{m}$ are currently being investigated as the systematic nature of the feature is suspicious (prime suspect is spectral calibration), given this is observed across scenarios and is not related to MHD activity which, for the pulses shown here, starts after the considered time-window.

The good match is seen across a wide set of limited, L-mode, NBI-heated discharges from the 2023 campaign.

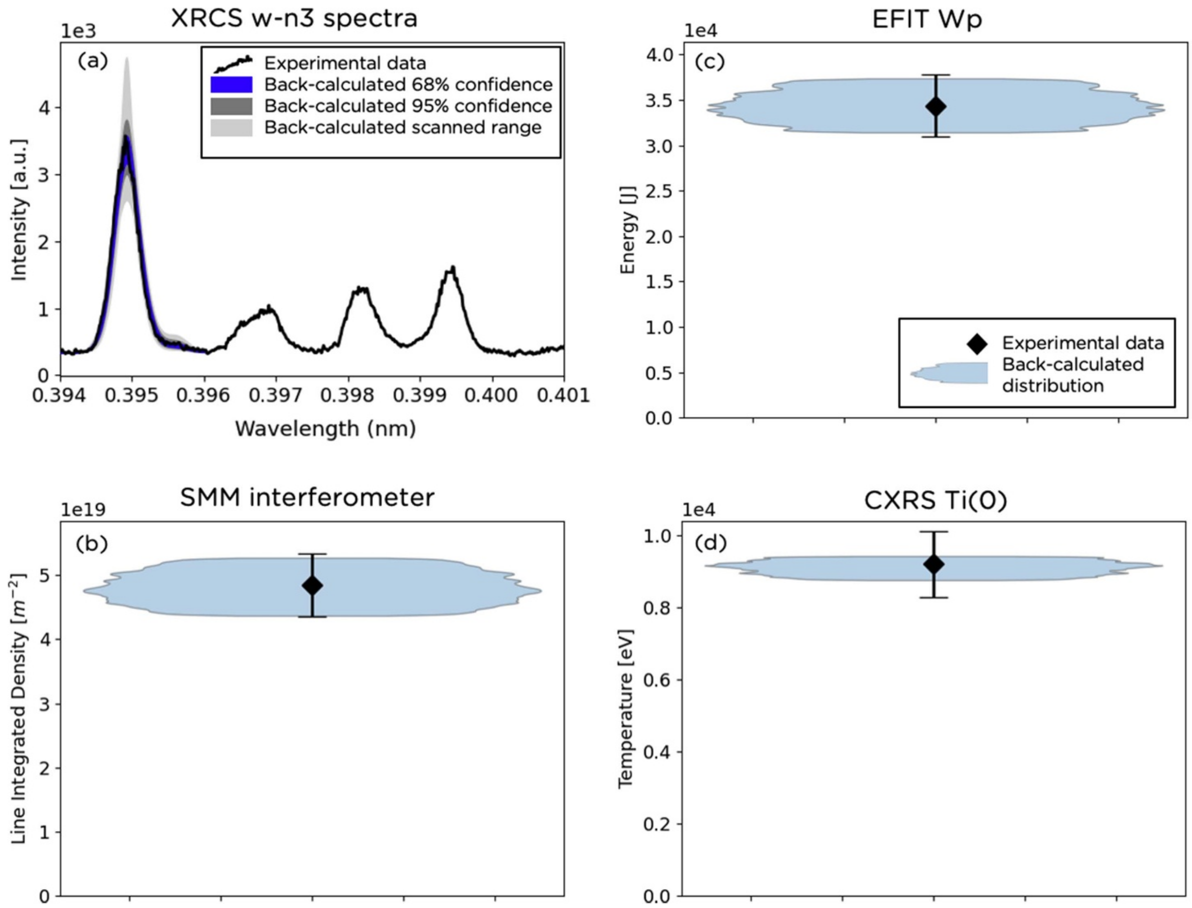

Figure 13. Comparison between experimental data (black) and the distribution (violin plots for b-d) of back-calculated values for the Bayesian inference workflow of the kinetic profile shapes for pulse 10 009 at 68 ms (kinetic profiles shown in figures 12(c) and (d): (a) XRCS spectra, (b) SMM interferometer, (c) EFIT stored energy, (d) central CXRS ion temperature).

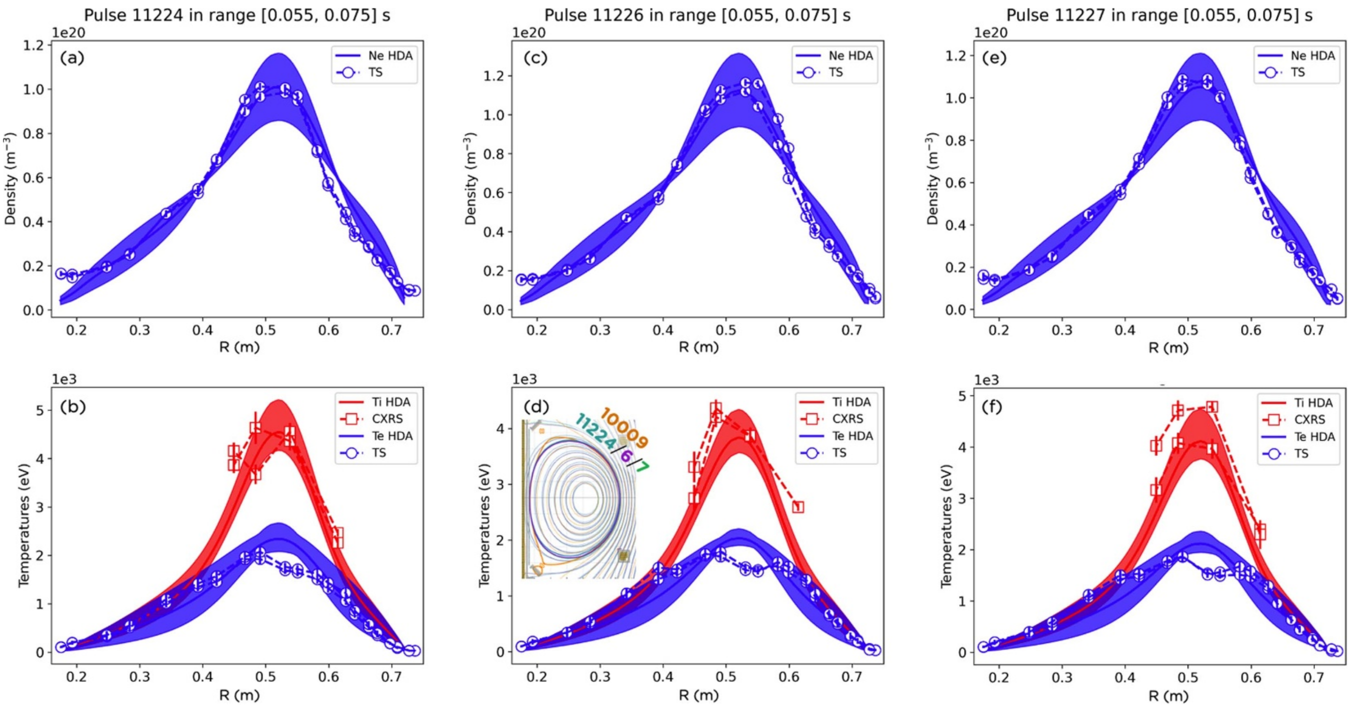

Figure 14. Comparison of HDA profile optimisation workflow vs TS and CXRS experimental data for recent 2023 plasma discharges using the same exact HDA code, assumptions and diagnostic data as in the analysis of the experiments from the 2021–22 campaign.

Additionally, TS shows how the electron density typically evolves from peaked to broad during the discharge, but almost always sitting within the HDA bounds. The TS electron temperature profiles are instead typically broad across the whole pulse, and well matched by the broad profile shape assumption used in HDA. This comparison further corroborates the results obtained during the 2021–22 campaign and the profile shapes used in the previous publications on ST40 data from those campaigns [1, 19, 35, 40–42].

5. Conclusions and outlook

Without aiming to provide a fully comprehensive account of all the diagnostic forward modelling activities taking place at Tokamak Energy, in this publication we have presented how some are used at TE to boost capabilities in diagnostic design, analysis methodology development, and data interpretation. Among the various applications discussed, in this section it is worth reviewing and reflecting upon the workflows used to constrain the plasma profile shapes.

Using simple models and workflows, including theory to constrain the unknowns, exploiting the collective knowledge of the team and external collaborators, it was possible to constrain the kinetic profile shapes using a minimal set of diagnostics, none of which were profile-capable. Defining strict boundary conditions for the validity of these profiles, they were released to the team for them to perform further work including theoretical modelling that could be compared with other experimental observations. This provided important feedback on how plausible these estimates were, and vital information on which steps to pursue next for future analyses, diagnostic and plasma scenario development. Meanwhile, the models and analysis workflows were upgraded and new diagnostics installed. The results of these new developments, shared in this publication, confirm the early work to a particularly high degree, substantiating the previous analysis and published work. They also endorse the philosophy of work, where MVPs are released early and further development carried out in successive waves.

The scope of this work evolves and adapts following the needs of the ST40 programme and of Tokamak Energy, its business and scientific milestones. With the new Thomson scattering [44], SXR [50] and bolometry cameras [51], neutron diagnostics [52], divertor IR camera and Langmuir probes [53–55] installed and commissioned on ST40, it is vital to arrive at a coherent picture of the measurements and interpretation from the plasma core to the edge. Until further upgrades to the CXRS system are in place, the ion temperature and toroidal rotation profiles will still require a certain level of inference. Full consistency between bolometry, unfiltered AXUV diodes and SXR cameras must provide a coherent picture of the core radiated power. This will feed into inference procedures to estimate the plasma composition, which is a key element to provide a closure for the neutron rate interpretation and to understanding turbulence stability. The estimation of power-balance will require all of the above, and will inform among other things divertor diagnostic interpretation and modelling.

In parallel, the diagnostic forward models are constantly being upgraded and their scope expanded. They are being employed to aid diagnostic design and commissioning, to test new analyses methodologies and to develop further integrated interpretation workflows. Predictive modelling results are fed into the framework to compare modelling directly with experimental data, providing a second, independent path to interpretation, understanding and optimisation, with the aim to streamline information flow, boost learning and speed up development towards the future.

Data availability statement

The data in the publication has been produced with the open-source software Indica which is publicly accessible on GitHub and can be accessed at anytime by the public. The data that support the findings of this study are available upon reasonable request from the authors.

Acknowledgments

Contributions from collaborators at Princeton Plasma Physics Laboratory and Oak Ridge National Laboratory were supported through U.S. Department of Energy CRADA NFE-19-07769. The authors would also like to thank Chris MacMackin (UKAEA) for his substantial contribution in creating the first version of *Indica*, much of which is still in use today, and S M Kaye (PPPL) for his invaluable contribution in the TRANSP interpretative analyses.

ORCID iDs

Marco Sertoli https://orcid.org/0000-0003-1528-6307
A Alieva https://orcid.org/0000-0002-4573-4951
P F Buxton https://orcid.org/0000-0002-0349-0434
H Lowe https://orcid.org/0000-0002-9085-1073
H V Willett https://orcid.org/0000-0002-4324-3438
Bart A Lomanowski https://orcid.org/0000-0003-2226-2004
O Marchuk https://orcid.org/0000-0001-6272-2605

References

[1] McNamara S *et al* 2023 *Nucl. Fusion* **63** 054002
[2] (Available at: https://github.com/ToFuProject/tofu)
[3] (Available at: www.raysect.org/)
[4] (Available at: https://github.com/cherab/core)
[5] (Available at: https://github.com/D3DEnergetic/FIDASIM)
[6] (Available at: https://euratom-software.github.io/calcam/html/index.html)
[7] (Available at: https://open.adas.ac.uk/)
[8] Svensson J and Werner A 2008 *Plasma Phys. Control. Fusion* **50** 085002
[9] Fischer R, Fuchs C J, Kurzan B, Suttrop W and Wolfrum E 2010 *Fusion Sci. Technol.* **58** 675–84
[10] Meneghini O and Lao L 2013 *Plasma Fusion Res.* **8** 2403009
[11] von Nessi G T and Hole M J 2013 *Rev. Sci. Instrum.* **84** 063505

[12] Langenberg A, Svensson J, Thomsen H, Marchuk O, Pablant N A, Burhenn R and Wolf R C 2016 *Fusion Sci. Technol.* **69** 560–7
[13] Pinches S *et al* 2019 *IAEA Technical Meeting on Fusion Data Processing, Validation and Analysis*
[14] Sciortino F *et al* 2021 *IAEA Technical Meeting on Fusion Data Processing, Validation and Analysis*
[15] Fischer R, Bock A, Burckhart A, Ford O P, Giannone L, Igochine V, Weiland M and Willensdorfer M 2019 *Nucl. Fusion* **59** 056010
[16] Callahan K, Chrystal C, Grierson B A, Haskey S R, Heidbrink W W and Herfindal J L 2019 *J. Instrum.* **14** C10002
[17] Schmuck S, Svensson J, Figini L, Micheletti D and Morales R B 2020 *Nucl. Fusion* **60** 066009
[18] Geiger B *et al* 2020 *Plasma Phys. Control. Fusion* **62** 105008
[19] Willett H, Osin D, Naylor G, Wood J, Lomanowski B and Sertoli M 2023 *J. Instrum.* **18** C03023
[20] Aimetta A, Moscheni M, Singh L, Marsden C, Scarabosio A, Sertoli M, Sladkomedova A, Subba F, Varje J and Wu H 2023 *Fusion Eng. Des.* **190** 113513
[21] (Available at: https://github.com/indica-mcf/Indica)
[22] Morita J *et al* Max Planck Institut fuer Plasmaphysik 1994 IPP III/199 (available at: https://core.ac.uk/download/pdf/210800245.pdf)
[23] Henderson S 2014 *PhD Thesis* University Of Strathclyde
[24] Boyle D 2016 Princeton University (available at: http://arks.princeton.edu/ark:/88435/dsp01fj236457r)
[25] Odstrčil T *et al* 2016 *Rev. Sci. Instrum.* **87** 123505
[26] Wesson J 1997 *Nucl. Fusion* **37** 577
[27] Sertoli M, Flanagan J, Maslov M, Maggi C, Coffey I, Giroud C, Menmuir S, Carvalho P, Shaw A and Delabie E 2018 *Rev. Sci. Instrum.* **89** 113501
[28] Sertoli M, Carvalho P J, Giroud C and Menmuir S 2019 *J. Plasma Phys.* **85** 905850504
[29] Marchuk O *et al* 2006 *Plasma Phys. Control. Fusion* **48** 1633
[30] Hill K W *et al* 2008 *Rev. Sci. Instrum.* **79** 10E320
[31] Sertoli M, Angioni C, Dux R, Neu R, Pütterich T and Igochine V 2011 *Plasma Phys. Control. Fusion* **53** 035024
[32] Schlummer T 2014 *PhD Thesis* University of Dusseldorf
[33] Sciortino F *et al* 2020 *Nucl. Fusion* **60** 126014
[34] von Hellermann M G *et al* 2005 *Phys. Scr.* **2005** 19
[35] Wood J, Lomanowski B, Delabie E, Willett H V, Sertoli M and Varje J 2023 *J. Instrum.* **18** C03019
[36] Meister H, Fischer R, Horton L D, Maggi C F, Nishijima D, Giroud C, Zastrow K-D and Zaniol B 2004 *Rev. Sci. Instrum.* **75** 4097–9
[37] Rathgeber S K, Fischer R, Fietz S, Hobirk J, Kallenbach A, Meister H, Pütterich T, Ryter F, Tardini G and Wolfrum E 2010 *Plasma Phys. Control. Fusion* **52** 095008
[38] Alieva A 2023 *MSc Thesis* University of York (UK)
[39] Breslau J *et al* 2018 *Princeton Plasma Phys. Lab.* (available at: www.osti.gov/biblio/1489900)
[40] Kaye S M, Sertoli M, Buxton P, Dnestrovskii A, McNamara S, Romanelli M and Thomas P 2023 *Plasma Phys. Control. Fusion* **65** 095012
[41] Ren Y, Kaye S M, Anastopoulos Tzanis M S, Sertoli M, Dnestrovskii A and Romanelli M 2023 *Plasma Phys. Control. Fusion* **65** 075007
[42] Duarte V, Gorelenkov N N, Kaye S M, Bonofiglo P J, Podestà M, Bland J, Buxton P, Gryaznevich M, Romanelli M and Sertoli M 2023 *Nucl. Fusion* **63** 036018
[43] Pereverzev G V *et al* 2002 *IPP-Report* 5/98
[44] Lowe H F *et al* 2023 *LAPD Conf.*
[45] Sertoli M *et al* 2023 *EPS Conf.*
[46] Asunta O *et al* 2023 *APS Conf.*
[47] Kaye S M *et al* 2023 *IAEA FEC Conf.*
[48] Sladkomedova A *et al* 2023 *IAEA FEC Conf.*
[49] McNamara S *et al* 2023 *IAEA FEC Conf.*
[50] Colgan C *et al* 2024 *HTPD Conf.*
[51] Harryman D *et al* 2024 *HTPD Conf.*
[52] Iliasona M V *et al* 2024 Characterisation of diamond and organic scintillation detectors utilising radiation sources for continuous plasma operation *Rev. Sci. Instrum.* submitted
[53] Moscheni M *et al* 2024 *PSI Conf.*
[54] Zhang X *et al* 2024 *PSI Conf.*
[55] Marsden C *et al* 2024 *PSI Conf.*